Influence of crystallization kinetics and flow behavior on structural inhomogeneities in 3D printed parts made from semi-crystalline polymers

Rene Sattler,[†,‡] Rui Zhang,[¶] Gaurav Gupta,[†,‡] Mengxue Du,[¶] Paul-Maximillian Runge,[§] Holm Altenbach,[§] René Androsch,[¶] and Mario Beiner*,[†,‡]

[†] *Fraunhofer Institute for Mikrostructure of Materials and Systems IMWS, Walter-Hülse-Str. 1, DE-06120 Halle (Saale)*

[‡] *Faculty of Natural Sciences II, Martin-Luther-University Halle-Wittenberg, Heinrich-Damerow-Str. 4, D-06120 Halle (Saale)*

[¶] *Interdisciplinary Center for Transfer-Oriented Research in Natural Sciences, Martin-Luther-University Halle-Wittenberg, Universitätsplatz 10, D-06108 Halle (Saale)*

[§] *Institute of Mechanics, Otto-von-Guericke-University Magdeburg, Universitätsplatz 2, D-39106 Magdeburg*

E-mail: mario.beiner@imws.fraunhofer.de

Abstract

We report the results of a study focusing on the influence of crystallization kinetics and the flow behavior on structural inhomogeneities in 3D printed parts made from polyamide 12 (PA12) and poly (lactic acid) (PLA) by Dynamic Mechanical Analysis (DMA), Differential Scanning Calorimetry (DSC), Fast Scanning Calorimetry (FSC)

https://doi.org/10.26434/chemrxiv-2024-82h74 **ORCID:** https://orcid.org/0000-0003-0459-323X

and Wide-Angle X-ray Diffraction (WAXD). Temperature-dependent WAXD measurements on the neat PLA filament reveal that PLA forms a single orthorhombic α phase during slow cooling and subsequent 2^{nd} heating. The PA12 filament shows a well pronounced polymorphism with a reversible solid-solid phase transition between the (pseudo)hexagonal γ phase near room temperature and the monoclinic α' phase above the Brill transition temperature $T_\mathrm{B} = 140$ °C. The influence of the print bed temperature T_b on structure formation, polymorphic state, and the degree of crystallinity χ_c of the 3D printed parts is investigated by height and depth dependent WAXD scans and compared with that of 3D printed single layers, used as a reference. It is found that the heat transferred from successive layers has a strong influence on the polymorphic state of PA12 since a superimposed mixture of γ and α phase is present in the 3D printed parts. In case of PLA a single α phase is formed. The print bed temperature has, in comparison to PA12, a major influence on the degree of crystallinity χ_c and thus the homogeneity of the 3D printed parts, especially close to the print bed. By comparing the obtained results from WAXD, DMA, DSC and FSC measurements with relevant printing times, guidelines for 3D printed parts with a homogeneous structure are derived.

Introduction

Additive manufacturing (AM) is commonly understood as a key factor in changing the economic landscape[1] in the next decades since it allows production in a decentralized system and a delivery on demand.[2] Fused Deposition Modeling (FDM) is one of the most popular AM methods[3] where a thermoplastic polymer- or metal filament is extruded through a heated nozzle on a print bed layer by layer. Compared to traditional manufacturing methods (i. e. injection moulding), crystallization in FDM or, to be more generally in AM, occurs step-wise during extrusion of the respective layer and not in bulk state. Thus internal structure formation processes are more complex since a vast variety of parameters, like print bed T_b and environment temperature or printing speed v, are important for the internal semi-crystalline structure of the final component.[3–8]

A significant influence on the internal structure of an FDM printed component has the print bed temperature T_b since a significant part of the crystallization process takes place when filament is deposited as shown by deJager et al. and Costanzo et al. on 3D printed Polyamide 12 (PA12) components.[3,4] It is also known that heat transferred from subsequent layers leads to non-isothermal processing conditions[4] of two adjacent filaments. Costanzo et al. have shown that the first printed layer of a PA12 component is thermally influenced by four subsequent printed layers. Only from the fifth layer onward, temperature induced by nozzle and melt no longer influences the first printed layer.[3] Other reports have shown that the temperature remains constant above the glass transition temperature T_g during printing and concluded that the maximum achievable degree of crystallinity χ_c is reached.[3,6,7] A further factor influencing the internal semi-crystalline structure of 3D printed poly(lactic acid) (PLA) components is the distance to the bed.[8] It is shown by Srinivas et al. that a large number of layers between component surface and bed cause a decreased heat transport of the bed due to high heat capacity and poor heat conduction of PLA resulting in a higher degree of crystallinity χ_c.[8]

Another interesting aspect is that PA12 and PLA are both polymorphic materials, which form different crystalline states, depending on processing conditions.[9–15] PA12 is obtainable in four crystalline phases that are the α, α' (monoclinic unit cell), γ and γ' ((pseudo)hexagonal unit cell) phases that can be distinguished by their characteristic d-spacings in the wide-angle X-ray diffraction (WAXD) region.[12–15] Recent studies indicated that 3D printed PA12 components crystallized preferentially in the (pseudo)hexagonal γ state.[4,5] PLA is achievable in the orthorhombic α-, α'-, and γ phase and the β phase with a frustrated structure.[9–11] Recent studies report that PLA components printed at low bed temperatures T_b crystallize in the α' phase[6,7] while samples printed at high bed temperatures T_b ($>$ 120 °C) have been found to crystallize in the stable α phase.[6]

A commonly applied criterion for the fluidity of polymeric filaments for FDM is to have a zero shear viscosity η_0 of about 10^2 to 10^3 Pa·s, depending on the filament used, at processing relevant temperatures above the melting temperature T_m.[16–20] This criterion gives a reasonable guideline for successful processing of related polymers but neglects the shear rate dependence of the fluidity of the polymeric melt. Since shear rates $\dot{\gamma}$ in the range of about $10^{\ 2}$ to 10^3 s^{-1} have to be expected in the nozzle[17,20] this is a relevant restriction that should be included in more detailed considerations.

Main goal of this study is to derive rational criteria which should be fulfilled to obtain homogeneous components without internal interfaces and macroscopic voids by FDM. Filaments from PLA and PA12 have been chosen as model systems since these polymorphic materials differ significantly regarding the crystallization rate in the processing relevant temperature range while their viscosities can be adjusted to be similar. We demonstrate that this results in different requirements regarding the parameters of the 3D-printing process and will end up with recommendations for the optimization of process parameters and material properties.

Materials and Methods

Materials Polyamide 12 (PA12) filament was purchased from Fiberlogy ©, Brzezie, Poland. The as-received filaments are transparent with a diameter of 1.75 mm. The PA12 has a melt flow index of 180 cm^3/10 min (235 °C/5 kg). Figure 1(b) shows the 2D scattering pattern along with the azimuthal integrated 1D scattering pattern of the as-received PA12 filament at room temperature as well as the 1D scattering pattern at 30 °C after slow cooling the relaxed melt. Three major Bragg reflections corresponding to the γ phase (hexagonal unit cell) indexed as 002, 004 and 100 can be seen at scattering vector q values of $q_{002} = 0.49$ Å^{-1}, $q_{004} = 0.79$ Å^{-1} and $q_{100} = 1.49$ Å^{-1}, respectively. The corresponding d-spacings ($d = 2\pi/q$) are $d_{002} = 12.82$ Å, $d_{004} = 7.95$ Å and $d_{100} = 4.22$ Å, respectively. The degree of crystallinity χ_c, using the areas of the crystalline peaks A_{cry} and the amorphous halo A_{amo}, is about 23 %.

Weak anisotropy in the intensity distribution of the 2D pattern is observed by local intensity maxima of the 002 reflection. The PA12 filament exhibits besides the hexagonal γ phase at room temperature a high temperature α' phase (monoclinic unit cell) above the Brill transition temperature T_B = 140 °C as shown in the results from temperature-dependent WAXD measurements in the Supplementary Information (cf. Figure SI1).

Poly (lactic acid) (PLA) filament (Renkforce ©RF-4511200) was purchased from Conrad Electronic SE, Hirschau, Germany. The as-received filament is transparent and its diameter is 1.75 mm. This grade contains $>$ 97.9 % PLA (CAS No. 26100-51-6), 2 % styrene/butadiene copolymer (CAS No. 9003-55-8) and $<$0.1 % other additives. The mass averaged molecular weight M_w and polydispersity index PI were measured by gel permeation chromatography (Omnisec, Malvern Panalytical, United Kingdom), against polystyrene standards to be 204 kg/mol and 1.4, respectively. Figure 1 (a) presents the 2D scattering pattern and the azimuthal integrated 1D scattering pattern of the PLA filament in the as received state along with the 1D scattering pattern at 30 °C after slow cooling the relaxed melt. The absence of Bragg reflections in the as-received filament reveals that the PLA filament is in the fully amorphous state. After slow cooling the relaxed melt PLA is present in the orthorhombic α phase, identified by two major reflections in the WAXD region along with further weak reflections. The major reflections are indexed as 200/110 and 203 occurring at $q_{200/110}$ = 1.18 Å^{-1} and q_{203} = 1.35 Å^{-1}. The corresponding d-spcaings are $d_{200/110}$ = 5.32 Å and d_{203} = 4.65 Å. Temperature-dependent WAXD measurements reveal that PLA forms a single orthorhombic α phase during step wise cooling the melt (cf. Figure SI2).

Differential Scanning Calorimetry (DSC). The crystallization kinetics of PA12 and PLA under non-isothermal and isothermal conditions were investigated using a heat-flux DSC 1 (Mettler-Toledo, Switzerland), which is equipped with a FRS 5 sensor and connected to a Huber Intracooler TC100. The purge gas was nitrogen with a flow rate of 60 mL/min. Sealed aluminum pans with a volume of 40 μL were used and the sample mass was about 4 mg. The first heating runs to determine the initial crystalline structure of PLA and PA12 filaments

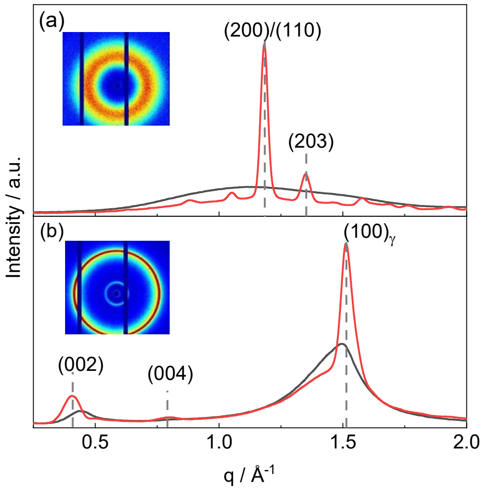

Figure 1: Scattering pattern of (a) PLA and (b) PA12 in the as received state (black) and measured at 30 °C after slow cooling the relaxed melt (red). The corresponding 2D scattering pattern of the as received filament are shown in the inset.

were performed with a heating rate of 20 K/min. More details of the temperature-time protocol will be discussed in the main text.

Fast Scanning Calorimetry (FSC). A Flash DSC from Mettler-Toledo, Switzerland, equipped with a chip-sensor (MultiSTAR UFS 1, Xensor-Integration, Netherlands) and a Huber intracooler TC100 was used for FSC measurements. The purge gas was nitrogen with a flow rate of 30 mL/min. A tiny particle with a sample mass of about 50 - 100 ng is placed on the FSC sensor. A good and stable thermal contact between the sample and the sensor was obtained after several melting-crystallization cycles. In non-isothermal measurements, cooling rates were varied between 10 and 5000 K/s and an optimum rate of 1000 K/s was applied for subsequent heating. Furthermore, isothermal crystallization of PA12 in the temperature range between 40 and 140 °C was investigated. The mass of FSC samples was estimated by the absolute, measured heat capacity difference at the glass transition temperature T_g of a fully amorphous sample, with the corresponding mass-normalized values available in the literature.[21,22]

Dynamic Mechanical Analysis. Dynamic mechanical measurements were performed on an AntonPaar MCR502 rheometer in plate-plate geometry (plate diameter 8 mm). Samples were prepared by pressing plates in a small mold using a heated hydraulic press (Collin) for approx. 4 min at 190 °C (PLA) and 260 °C (PA12) with a pressure of 2 bar to form a disc with a diameter of 24.5 mm and a height of $\approx$ 1 mm. Subsequently, a specimen with a diameter of 8 mm was punched out of the disc. Before measured, the specimen was placed between the plates in a pre-heated chamber (190 °C PLA and 210 °C PA12) and homogenized with a shear deformation of 1 %. After homogenization, the gap between the plates was reduced to approx. 0.7 mm. Isothermal frequency sweeps were measured during step-wise cooling between 210 and 150 °C for PLA and between 210 and 180 °C for PA12 in steps of 10 K. Frequency sweeps were performed in a frequency range 0.01 - 100 rad/s with a shear strain of 2 % at constant temperature. Master curves were constructed by TA Orchestrator software.

3D-printing. FDM parts were manufactured on a *A4v4* printer by 3ntr with a multi-material high temperature hotend print head (with three nozzles) with diameter of 0.4 mm on a heated carbon fiber reinforced polymer (CFPR) built plate. Using Simplify3D software, a CAD file (constructed in 3ds CATIA V5) was sliced and exported as G-Code file. After compilation, the G-Code was sent to the 3ntr Print Server where printing parameters were set. Table 1 presents nozzle temperature T_n, print bed temperature T_b, printing speed v, width of layer w_l, height of layer z_l, extrusion multiplier E_m, total height of component z and height of the filled part z_f, used for printing of PA12 and PLA components. E_m was used for optimization of the extrusion flow rate to obtain best results when depositing the filament.

Table 1: Printing parameters and dimensions of the 3D-printed components

Material	T_n	T_b	v	w_l	z_l	E_m	z	z_f
[-]	[°C]	[°C]	[mm/s]	[mm]	[mm]	[%]	[mm]	[mm]
PA12	260	30, 80, 120	50	0.55	0.30	80	60	20
PLA	190	30, 60, 90	50	0.55	0.30	100	60	20

The dimensions of the 3D-printed half-cylinders are: height $z = 60$ mm, diameter $y = 30$ mm and depth $x = 15$ mm. The printed part consists of a filled core region up to a height z of

20 mm while the height z of the hollow part is 40 mm with a wall thickness of 2 mm (Figure 2(a)). Printing of the components was divided into two stages - printing of perimeter and filling stage. In total, eight perimeter were printed from most inner to outermost perimeter, followed by the filling stage with an angle of ± 45° (Figure 2(b)). In order to ensure sufficient adhesion between extruded filament and print bed, a layer of painter's tape with a thin film of water diluted wood glue (1:1 ratio) was attached to the print bed. The Z-offset between nozzle and print bed was 2 mm. The single layers of PLA and PA12 were also printed with the same printing parameters as used for printing the respective components, i.e., an analogous waiting period was applied before the component was removed from the bed.

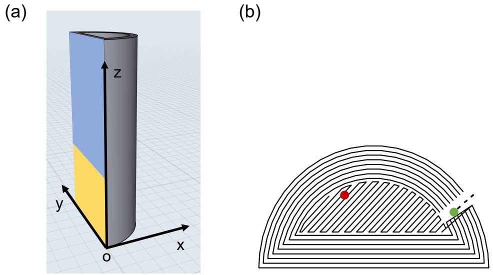

Figure 2: (a) CAD drawing of the chosen model component with coordinate system. (b) Top view on one layer. Trace of nozzle starting with inner most perimeter (green dot) printing to outer most perimeter, followed by filling stage in angle of ± 45°. End point of layer printing is indicated by red dot.

Microtomy. In a first step, the 3D-printed components were separated into two parts - filled part ($0 \leq z \leq 20$ mm) and hollow part ($20 \leq z \leq 60$ mm) (Figure 3(a)). The filled part was clamped in the holding device of the microtome with the flat side of the half cylinder, aligned parallel to the knife of the microtome (Figure 3(b)). Subsequently, thin sections were then gradually prepared by the microtome with a thickness of 100 μm.

X-ray Diffraction. X-ray diffraction experiments were performed in transmission mode using a SAXSLAB laboratory setup (Retro-F) equipped with an AXO microfocus X-ray source with an AXO multilayer X-ray optic (ASTIX) as monochromator for CuK$_\alpha$ radiation ($\lambda = 1.54$ Å) . A DECTRIS PILATUS3 R 300K detector was used to record the 2D scatter-

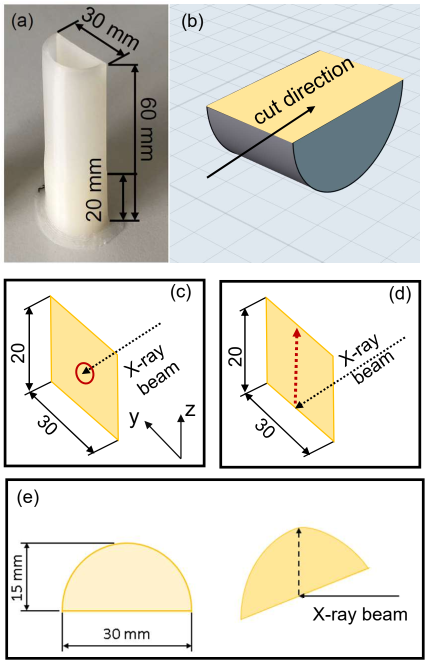

Figure 3: (a) 3D-printed component consisting of an lower filled part ($z \leq 20$ mm) and a upper hollow part (20 mm $\leq z \leq$ 60 mm); (b) CAD model of the filled part of 3D-printed components for microtomy; (c) Microtomed thin section for depth dependent measurement. The red circle shows the point of measurement at $y = 15$ mm and $z = 10$ mm (10 mm from bottom); (d) Thin section used for height dependent measurements along the red dashed line (fixed $x = 2.5$ mm and $y = 15$ mm) from $z = 0$ mm to $z = 20$ mm; (e) Single layer and direction of scanning to study the depth dependence at from $x = 0$ mm to 15 mm.

ing pattern. The sample to detector distance was about 10 cm. A twin pinhole system was used for the measurements with an aperture size of 0.9 mm and 0.4 mm. Calibration of the sample-detector distance was performed using a silver behenate standard.

Temperature dependent WAXD measurement on the as received filament samples were performed using a Linkam hot stage. The samples were placed in a small hole in an aluminum disc having a diameter of 2 mm. The temperature range for PLA was T = 30 °C to 190 °C while for PA12 the measured temperature range was from T = 30 °C to 260 °C in steps of 10 K. The heating and cooling rate between temperatures was set as ± 10 K/min. The measurement time at each temperature was 5 minutes. The first heating run was performed to erase the thermal history of the filaments.

WAXD measurements on the thin sections (about 100 μm thick) were performed at room temperature. To study the depth dependence, thin sections taken from different depth x were mounted on the Linkam stage so that the center of the section (z = 10 mm, y = 15 mm) was located in the beam (Figure 3(c)). In order to investigate structural heterogeneities in 3D-printed components depending on the distance to the bed, height dependent scans were performed on thin sections at room temperature (Figure 3 (d)). The measurements were performed at fixed x = 2.5 mm and y = 15 mm position over the entire height of filled part from z = 0 mm to 20 mm with a step size of 0.6 mm. To investigate the influence of the print bed temperature T_{b} on a single 3D-printed layer, scans along the x direction (depth) were performed from x = 0 mm to 15 mm with a step size of 0.75 mm as shown in Figure 3 (e).

Data evaluation and analysis was performed using OriginLab 2019b. In order to fit the WAXD data, a Gaussian-Lorentz cross fit function was applied to determine the area of the amorphous halo A_{amo} and Bragg reflections A_{cry} (cf. Figure SI2, SI4 and SI5). The region of integration for PLA and PA12 was $0.5\ \text{Å}^{-1} \leq q \leq 2.0\ \text{Å}^{-1}$ and $1.0\ \text{Å}^{-1} \leq q \leq 2.0\ \text{Å}^{-1}$, respectively. Representative fit examples of the WAXD data can be found in the SI Figure

SI4 and SI5. The degree of crystallinity χ_c is calculated from

$$\chi_c = \frac{\sum A_{cry}}{\sum A_{cry} + A_{amo}} \tag{1}$$

where ΣA_{cry} is the total peak area of all relevant Bragg reflections while A_{amo} is the area of the amorphous halo.

Results

Crystallization kinetics

In Figure 4(a), FSC heating scans of PA12, after prior cooling from 220 to -60 °C at rates varying from 1 to 5000 K/s, are plotted. The enthalpy of crystallization during prior cooling is estimated through (1) integrating the curves in the temperature range from 110 to 200 °C and then (2) dividing the obtained value by the heating rate applied (1000 K/s). A straight line is applied as the baseline. In Figure 4(b), the heat flow for PA12 during isothermal crystallization is shown. The time that heat flow reaches a maximum is determined as peak-time of crystallization. In Figure 5(a), DSC heating scans of PLA, after prior cooling from 200 to 25 °C at rates varying between 0.017 to 0.33 K/s, are plotted. Similar to PA12, the enthalpy of crystallization during prior cooling is estimated through (1) integrating the curves in the temperature range from around 125 to 190 °C and then (2) dividing the obtained values by the heating rate applied (0.33 K/s). Also here, a straight line is used as baseline. Figure 5(b) shows the heat flow as a function of time at temperatures between 73 °C to 124 °C. Similar as in the case of PA12, the time that heat flow reaches maximum is determined as peak-time of crystallization.

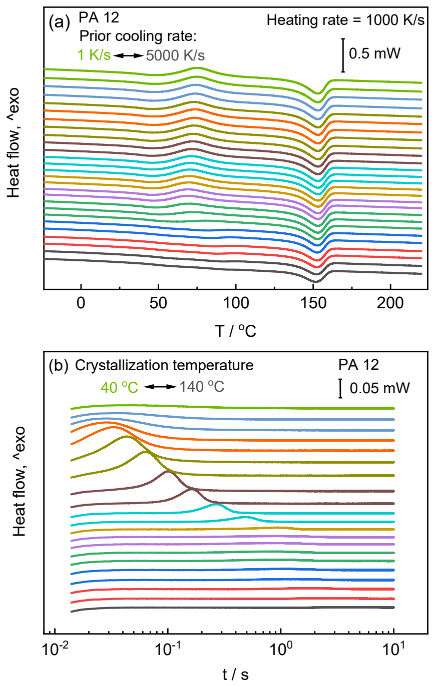

Figure 4: (a) FSC heating scans of PA12 with a heating rate of 1000 K/s after cooling with different rates from 1 to 5000 K/s. (b) Isothermal FSC scans at crystallization temperatures between 40 °C and 140 °C.

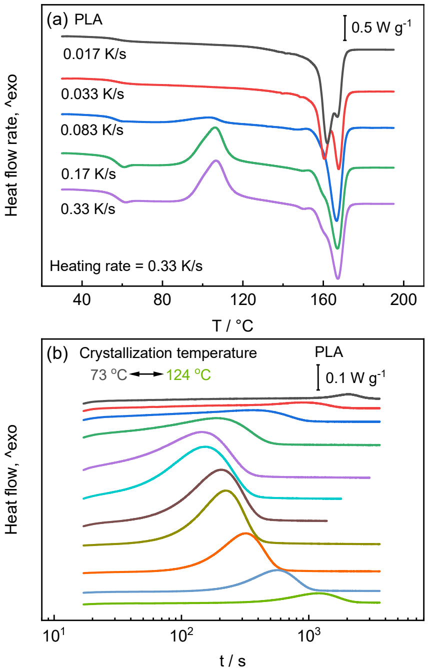

Figure 5: (a) DSC heating scans for PLA at a heating rate of 0.33 K/s after cooling with rates between 0.017 to 0.33 K/s. (b) Isothermal DSC scans at temperatures between 73 °C and 124 °C.

The non-isothermal crystallization kinetics of PLA and PA12 are evaluated through the crystallinity as a function of the prior cooling rate, as shown in Figure 6(a), according to the procedure reported in the literature.[23,24] When the cooling rate is above 0.17 K/s, negligible crystallization occurs during cooling of PLA while, for PA12, crystallization is absent during cooling faster than 100 K/s. Then, critical cooling rates to suppress crystallization are determined as 0.17 K/s and 100 K/s for PLA and PA12, respectively. Comparing both, it can be seen that the maximum crystallization rate of PA12 is much higher than in case of PLA. Isothermal crystallization kinetics of PLA and PA12 are evaluated through the peak-time of crystallization as a function of crystallization temperature, as shown in Figure 6(b).

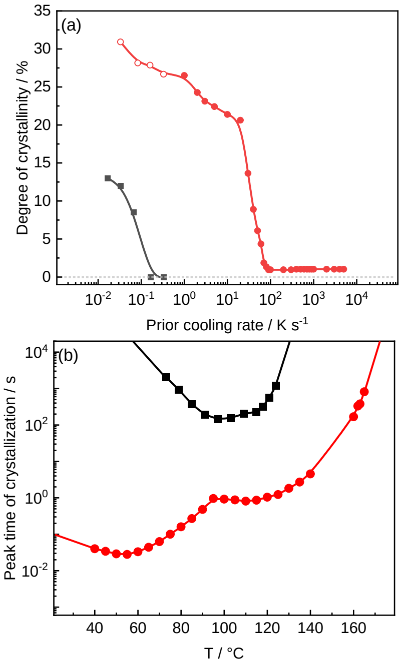

Figure 6: (a) Enthalpy based crystallinity of PLA (black) and PA12 (red) as a function of cooling rate from non-isothermal crystallization. The red open circles are the degree of crystallinity, determined in non-isothermal DSC measurements. The values of $\Delta H_{m,100}$ to determine the degree of crystallinity are 104 J/g (PLA)[23] and 4.184 × 50 J/g (PA12)[25] (b) Peak time of crystallization as a function of temperature in the temperature range from 73 °C to 124 °C for PLA and between 40 °C to 140 °C for PA12.

The peak-time of crystallization represents the crystallization rate at the particular crystallization temperature. PA12 shows a bimodal dependence of the crystallization time on temperature with minima at about 5 °C and 115 °C, respectively. Unlike PA12, a distinct bimodal dependence cannot be seen in the crystallization times as a function of temperature for PLA. Only a weak kink at around 110 °C points to the formation of α'- and α-crystals at low and higher temperatures with different kinetics, respectively. Comparing PLA and PA12, it proposes that the crystallization times under isothermal conditions for PA12 are commonly much shorter than those of PLA.

Flow behavior in the molten state

Isothermally measured scans for the shear storage $G^{'}$ and loss modulus $G^{''}$ as function of angular frequency ω, $G^{'}(\omega)$ and $G^{''}(\omega)$, in the flow transition region of PA12 are shown in Figure 7(a). The cross-over point of $G^{'}(\omega)$ and $G^{''}(\omega)$ can be associated with the transition from the rubbery to the liquid-like state. Hence, temperature-dependent terminal relaxation times τ_{r} can be estimated from the cross-over frequencies ω_{C} according to $\tau_{\mathrm{r}} = 1/\omega_{\mathrm{C}}$. The intercept shifts like the entire flow transition range to lower frequencies ω with decreasing temperature since relevant motions slow down and the terminal relaxation time τ_{r} increases. Note that terminal flow behavior is not achieved in the investigated frequency window for PA12 up to 210 °C.

The Arrhenius plot in Figure 7(b) demonstrates that $-log(\tau_{\mathrm{r}})$ is decreasing nearly linearly with reciprocal temperature $1000/T$ in the investigated temperature range. An activation energy of $E_{\mathrm{A}} = 74.9\,\mathrm{kJ/mol}$ is taken from an Arrhenius fit according to $\tau_{\mathrm{R}} = A * exp(E_{\mathrm{A}}/RT)$. The activation energy E_{A} denotes the energy barrier, that has to be overcome to achieve a viscous flow, i.e., the polymer is transferred in the relaxed melt. This may an important quantity if one is considering that crystallization should take place within the layers in order to achieve a homogeneous structure in all directions of the component. Note that the temperature dependence of terminal relaxation times should follow a Vogel-Fulcher-Tammann-Hesse (VFTH) behavior. However, a corresponding fit is not possible here due to a limited temperature range between crystallization and degradation temperature in case of PA12. The Arrhenius law is used as zeroth approximation to extrapolate terminal relaxation times τ_{r} at processing relevant temperatures. In Table 2 terminal relaxation times τ_{r} as well as horizontal shift factors a_T from a master curve construction are compiled. In Figure 7(b) the shift factors -$log(a_{\mathrm{T}})$ are also plotted as function of 1000/T giving an activation energy $E_{\mathrm{A}} =$ 60.9 kJ/mol, which is slightly deviating from the value obtained from temperature dependent terminal relaxation times τ_{r}. This indicates the existence of experimental uncertainties in case of data for only four temperatures. Figure 8(a) shows $G^{'}$ and $G^{''}$ isotherms for PLA measured at temperatures from 210 °C to 150 °C. Terminal relaxation times τ_{r} are determined from the intercept $G^{'}(\omega) = G^{''}(\omega)$ where available and listed in Table 2 together with temperature-dependent values for horizontal shift factor a_{T} as obtained from a master curve construction. In Figure 8(b) the logarithm of shift factors $-log(a_{\mathrm{T}})$ and terminal relaxation times $-log(\tau_{\mathrm{r}})$ is plotted as function of $1000/T$ together with Arrhenius fits giving activation energies of $E_{\mathrm{A,aT}} = 35.7$ kJ/mol and $E_{\mathrm{A},\tau_{\mathrm{r}}} = 40.5$ kJ/mol, respectively. In case of shift factors a_{T} the measured temperature interval for PLA is broad enough to apply the Vogel-Fulcher-Tammann-Hesse (VFTH) equation[26]

$$-log(a_T) = log(A) - \frac{B}{T_V - T} \tag{2}$$

Table 2: Terminal relaxation times τ_{r} and shift factors a_T for PA12 and PLA

PA12			
T [°C]	$1000/T$ [1000/K]	τ_{r} [s]	a_{T} [a.u.]
210	2.07	0.01	1.00
200	2.11	0.03	2.30
190	2.16	0.06	4.29
180	2.21	0.23	10.59
PLA			
210	2.07	-	1.00
200	2.11	-	1.31
190	2.16	-	1.93
180	2.21	-	2.98
170	2.26	0.01	4.88
160	2.31	0.02	8.89
150	2.36	0.03	18.31

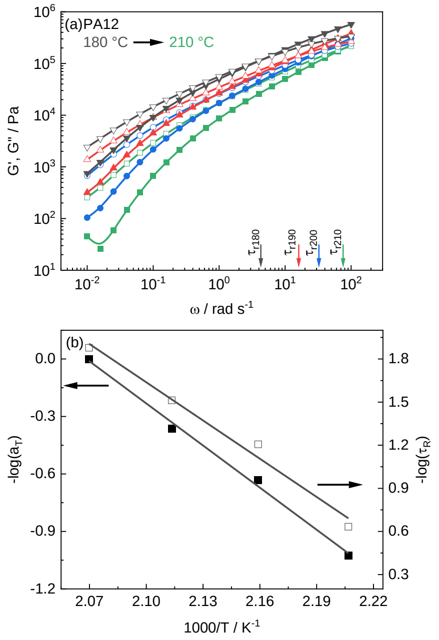

Figure 7: (a) Isothermal sweeps for storage modulus G' (closed symbols) and loss modulus G'' (open symbols) of PA12 as function of angular frequency ω for temperatures between 210 °C and 180 °C. Terminal relaxation time τ_r at crossover modulus G_c of the respective temperature indexed with a colored arrow on the ω-axis; (b) Arrhenius plot of -*log* a_T (closed symbols) and -*log* τ_r (open symbols) vs. $1000/T$ for PA12. The solid line is an Arrhenius fit corresponding to an activation energy $E_\mathrm{A} =$ 60.9 kJ/mol and 74.9 kJ/mol, respectively.

which is commonly used to describe the temperature dependence of the flow transition. The Vogel-temperature T_V is typically about 50 K below the glass transition temperature T_g and is associated to the temperature where the viscosity becomes infinite.[26] A VFTH fit to the shift factors a_T for PLA gives $A = 16.9$ for the prefactor, $B = 2.6$ K for the curvature and $T_\mathrm{V} = 331$ K for the Vogel temperature. Surprisingly the Vogel temperature T_V is in the same range as the glass transition temperature T_g of PLA (comp. $T_\mathrm{g} = 330$ K) and not about 50 K below the glass transition temperature as typically reported in literature ($T_\mathrm{V,lit} = 277$ K - 296 K).[27]

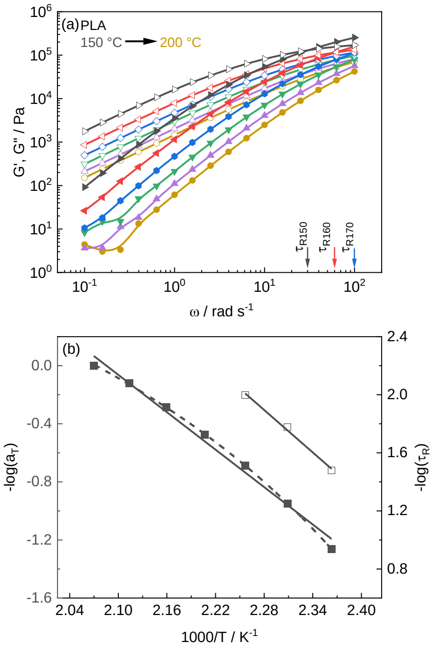

Figure 8: Isothermal sweeps for storage modulus G' (closed symbols) and loss modulus G'' (open symbols) for PLA as function of angular frequency ω for temperatures between 200 °C and 150 °C. Terminal relaxation time τ_r of the respective temperature are indexed with colored arrows on the ω-axis. (b) Arrhenius plot $-log(a_\mathrm{T})$ (closed symbols) and $-log(\tau_\mathrm{r})$ (open symbols) vs. $1000/T$ for PLA. The solid line is an Arrhenius fit corresponding to activation energies $E_\mathrm{A} = 35.7$ kJ/mol and 40.5 kJ/mol, respectively. The dashed line represents a VFTH fit.

Semi-crystalline structure of 3D printed components

Polyamide 12 Height-dependent WAXD scans are performed on thin sections microtomed in a depth of 2.5 mm from the filled part of the components and scanned from bottom $z = 0$ mm to 20 mm in steps of 0.6 mm in the middle of the thin section ($y = 15$ mm). Figure 9(a) shows a comparison of representative 1D scattering pattern measured at a height of 0.6 mm for PA12 components printed at print bed temperatures T_b of (a) 30 °C, (b) 80 °C and (c) 120 °C. The WAXD pattern show for all bed temperatures a characteristic reflection at low q values assigned to the (002) plane at $q_{002} = 0.42$ Å^{-1} and $q_{004} = 0.8$ Å^{-1}. The reflection is corresponding to layered H-bonds along the chain axis, as typically observed for polyamides.[28–31] In the WAXD range, the pattern for 3D-printed PA12 parts show one strong Bragg reflection, corresponding to the (100) plane of the (pseudo)hexagonal γ phase observed at $q_{100} = 1.52$ Å^{-1}. The corresponding d-spacing is $d_{100} = 4.13$ Å. Two additional reflections occur as shoulders at $q = 1.44$ Å^{-1} and $q = 1.59$ Å^{-1}. The latter reflections can be attributed to the (200) and (010) planes of the α phase, respectively.[32]

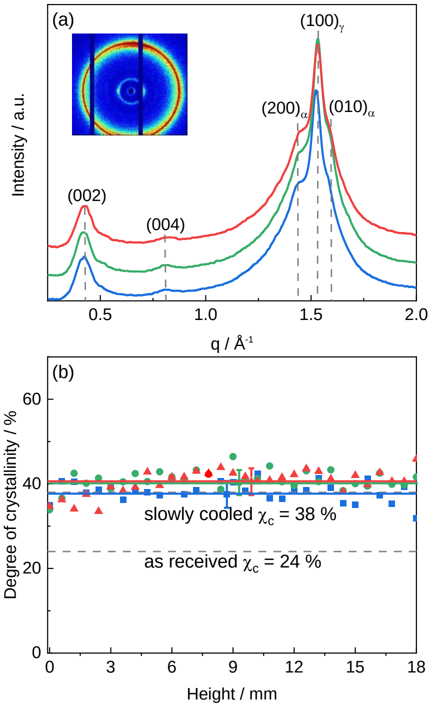

Figure 9: (a) Representative 1D WAXD scattering pattern for PA12 components printed at T_b = 30 °C, 80 °C and 120 °C at a height of $z = 0.6$ mm ($x = 2.5$ mm and $y = 15$ mm are fixed). The inset shows a representative 2D scattering pattern (T_b = 30 °C) exhibiting a anisotropic intensity distribution. (b) Degree of crystallinity χ_c as function of height z. The degree of crystallinity χ_c of the as received- and slowly cooled PA12 from temperature dependent WAXD scans is indicated by gray dashed lines. Error bars correspond to the standard derivation of mean values from height dependent measurement.

A comparison with scattering pattern of slowly cooled PA12 (Figure SI1(a) and (b)) reveals that the positions of the (200) planes almost match. However, the q_{010} value for the 3D printed component does not agree with that of the (010) plane for the α'-phase, which suggests the appearance of the α phase. Hiramatsu et al. have reported that a mixture of γ'- and α phase is formed by drawing the γ phase of PA12 above 70 °C.[32] The 1D pattern observed in this case are in approximate agreement with those for the investigated 3D printed component in Figure 9(a).[32] This suggests that a mixed structure containing γ and α phases occurs in the investigated 3D printed components made from PA12.

Structural parameters including the α - to - γ ratio $R_{\gamma/\alpha}$ are determined by an approximation of diffraction pattern based on the fit results. The values obtained at a height of $z = 0.6$ mm for different print bed temperatures T_b are given in Table 3. The values for the coherence length of the γ phase L_{100} for $T_\mathrm{b} = 30$ °C of about 12.3 nm are in good agreement with those found in temperature-dependent measurements, while L_{100} is increasing to 12.7 and 13.2 nm for higher print bed temperatures T_b (80 °C, 120 °C) indicating the occurrence of slightly larger crystalline domains. Considering the γ-to-α ratio and the overall degree of crystallinity $\chi_\mathrm{c,tot}$ ($36 - 41$ %) dependence on T_b, one can conclude, that the print bed temperature T_b has a weak influence on the crystalline state close to the print bed for PA12. In Figure 9(b) the overall degree of crystallinity χ_c is plotted *vs.* height z for print bed temperatures T_b of 30 °C, 80 °C and 120 °C (at the same x and y position). The degree of crystallinity χ_c is not only near to the bed similar but also for larger heights z approximately the same for all three print bed temperatures T_b (about 40 %). Nevertheless, the average degree of crystallinity χ_c far from the print bed is seemingly very few percent higher for the higher T_b values, even if a scatter in the data is within the experimental error range. Slight differences depending on T_b can also be seen in the γ-to-α phase ratio. The mean fraction of the α phase at print bed temperatures T_b of 30 °C and 80 °C is with 0.43 and 0.44 similar but a significant increase to 0.52 is found for $T_\mathrm{b} = 120$ °C. Depth-dependent WAXD studies are performed by measuring microtomed thin sections taken from the filled

Table 3: Structural parameters characterizing the local crystalline state of differently 3D-printed PA12 components

		α phase				γ phase				
position	T_b	q_{200}	q_{010}	d_{200}	d_{010}	q_{100}	d_{100}	L_{100}	$\chi_\mathrm{c,tot}$	ratioγ/α
	[°C]	[Å^{-1}]	[Å^{-1}]	[Å]	[Å]	[Å^{-1}]	[Å]	[Å]	[%]	[-]
$x = 2.5$ mm, $y = 15$ mm,	30	1.43	1.58	4.38	3.97	1.52	4.12	122.7	41	1.09
$z = 0.6$ mm	80	1.44	1.57	4.37	3.99	1.53	4.11	126.9	36	1.35
from height dependent scans	120	1.44	1.59	4.36	3.95	1.53	4.10	132.6	36	0.57
$x = 0.1$ mm, $y = 15$ mm	30	1.43	1.55	4.39	4.05	1.51	4.16	109.3	36	1.16
$z = 10$ mm	80	1.47	1.58	4.29	3.98	1.53	4.12	108.9	43	1.29
from depth dependent scans	120	1.44	1.58	4.38	3.97	1.52	4.12	113.6	44	0.86

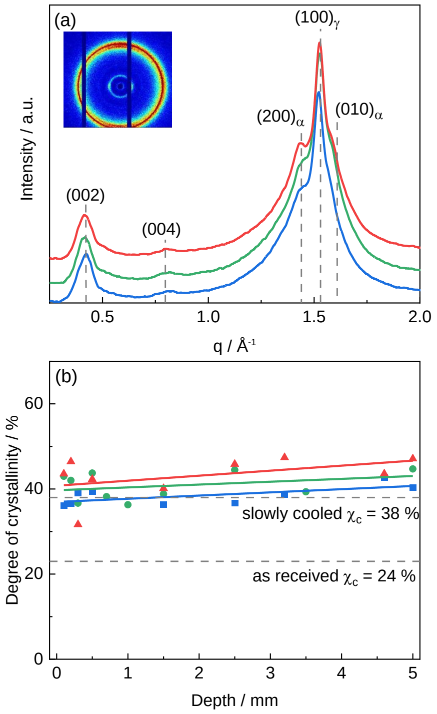

Figure 10: (a) Representative WAXD pattern for PA12 components printed at $T_\mathrm{b} = 30$ °C, 80 °C and 120 °C at a depth of $x = 2.5$ mm and fixed values for $z = 10$ mm and $y = 15$ mm. The inset shows a representative 2D scattering pattern ($T_\mathrm{b} = 30$ °C) exhibiting an anisotropic intensity distribution. (b) Degree of crystallinity as a function of the depth x of the 3D-printed PA12 components. The degree of crystallinity χ_c for the slowly cooled and as received PA12 is indicated by dashed lines.

part of 3D-printed PA12 components ($y = 15$ mm and $z = 10$ mm are fixed) at various depths from $x = 0.1$ mm to 5.0 mm approaching the core of the half cylinder. Figure 10(a) shows representative 1D scattering pattern for thin sections taken at a depth of $x = 2.5$ mm for PA12 components printed at different print bed temperatures T_b. The 1D WAXD pattern are similar to those obtained from the height-dependent measurements and confirm the coexistence of α and γ phases. A prominent change is, however, that the $q_{(200)}$ reflection at 1.43 Å^{-1} is becoming more pronounced with increasing print bed temperatures T_b. The 2D scattering pattern (inset of Figure 10(a)) basically support the conclusion which has been derived before from height dependent measurements. For all investigated depths local intensity maxima at meridional positions are observed for the α phase while the q_{100} reflection representing the γ phase shows basically a isotropic intensity distribution. In Figure 10(b) the degree of crystallinity χ_c is plotted as a function of depth x for PA12 components printed at different print bed temperatures T_b. In average, the degree of crystallinity χ_c is slightly higher as compared to the value observed for PA12 samples after slow step-wise cooling ($\chi_\mathrm{c} = 38$ %). Moreover, a certain increase in χ_c is observed with increasing depth x approaching the core of the component as well as with increasing print bed temperature T_b. In addition, the fraction of α phase is also weakly increasing from 0.47 at $T_\mathrm{b} = 30$ °C to 0.52 for $T_\mathrm{b} = 120$ °C. Structural parameters derived from a detailed peak analysis and fitting of the 1D WAXD data for the outer layer ($x = 0.1$ mm) and more close to the core ($x = 2.5$ mm) of the component are compared in Table 3. The reported parameters clearly indicate that the semi-crystalline state of the PA12 components at these positions is basically unaffected by the print bed temperature T_b. Only weak changes in the degree of crystallinity χ_c and coherence length L with print bed temperature T_b are observed.

Poly(lactic acid) The height dependence of the local crystalline state is investigated based on thin sections microtomed from PLA components parallel to the x-y plane, similar to the 3D-printed PA12 components. Figure 11(a) shows representative scattering pattern for a height of $z = 0.6$ mm measured on sections taken from PLA components printed at three different print bed temperatures T_b. Depth and width coordinates are kept constant ($x = 2.5$ mm and $y = 15$ mm). Two major reflections that are assigned to the (200)/(110) and (203) planes are observed for all print bed temperatures T_b at $q_{200/110} = 1.18$ Å^{-1} and $q_{203} = 1.35$ Å^{-1}. The corresponding d-spacings are $d_{200/110} =$ Å 5.32 and $d_{203} = 4.65$ Å. In addition, weaker reflections are commonly found (cf. Figure 11(a)). Note, however, that these reflections are extremely weak near the printing bed up to a height of $z = 5$ mm for $T_\mathrm{b} =$ 30 °C and 60 °C. As in the case of step-wise cooling (cf. Figure SI3(a)) crystallization in 3D-printed PLA occurs always in the orthorhombic α phase with comparable unit cell dimensions ($a = 10.62$ Å, $b = 6.13$ Å and $c = 29.00$ Å). Table 4 contains structural parameters as obtained from a peak fitting analysis of the corresponding 1D scattering pattern. The results clearly evidence that the local degree of crystallinity χ_c increases strongly with increasing print bed temperature T_b. The 2D scattering pattern like exemplary shown in the inset of Figure 11(a) demonstrate that an isotropic intensity distribution is found for 3D-printed PLA components indicating that there is no preferred molecular orientation in conjunction with a relaxation of the initially oriented strand. Figure 11(b) presents the degree of crystallinity χ_c as function of the height z for PLA components printed at different print bed temperatures T_b. A clear increase in the degree of crystallinity χ_c with print bed temperature T_b is found, especially close to the print bed. For low print bed temperatures ($T_\mathrm{b} \leq 60$ °C) the degree of crystallinity χ_c increases linearly with height up to $z = 6$ mm and then reaches a saturated value of about 30 %. For $T_\mathrm{b} = 90$ °C, the degree of crystallinity χ_c saturates already at $z \approx$ 2 mm and reaches a slightly higher degree of crystallinity χ_c of about 34 %. The degree of

Table 4: Structural parameters characterizing the local crystalline state of differently 3D-printed PLA components.

position	T_b	$q_{200/110}$	q_{203}	$d_{200/110}$	d_{203}	$L_{200/110}$	L_{203}	χ_c
	[°C]	[Å^{-1}]	[Å^{-1}]	[Å]	[Å]	[Å]	[Å]	[%]
$x = 2.5$ mm, $y = 15$ mm	30	1.18	1.35	5.31	4.65	171.2	175.0	6
$z = 0.6$ mm	60	1.180	1.35	5.32	4.67	181.1	162.9	12
from height dependent scans	90	1.18	1.34	5.32	4.67	185.9	150.3	21
$x = 0.1$ mm, $y = 15$ mm	30	1.17	1.34	5.36	4.70	261.8	208.1	32
$z = 10$ mm	60	1.18	1.35	5.31	4.65	168.9	137.8	30
from depth dependent scans	90	1.19	1.36	5.29	4.64	183.7	157.1	29

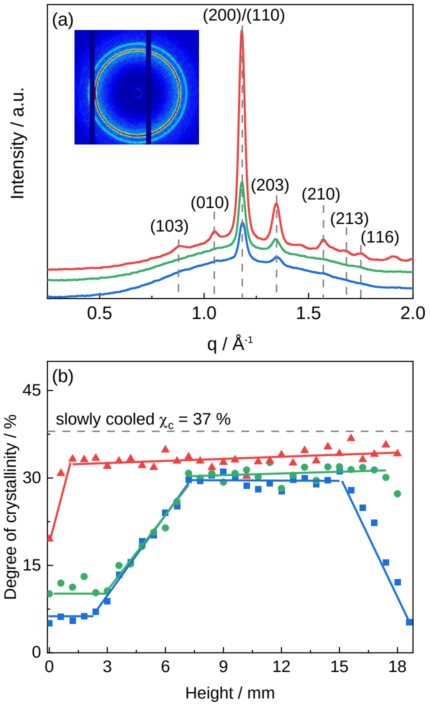

Figure 11: (a) Representative WAXD scattering pattern of PLA components printed at T_b = 30 °C, 60 °C and 90 °C at a height of $z = 0.6$ mm ($x = 2.5$ mm and $y = 15$ mm are fixed). The inset shows a representative 2D scattering pattern (T_b = 30 °C) exhibiting a isotropic intensity distribution. (b) Degree of crystallinity χ_c as function of height z. The degree of crystallinity χ_c of slowly cooled PLA is indicated by a dashed line.

crystallinity χ_c near the core of the component seems to depend only slightly on the print bed temperature T_b. In general, the observed trends underline the strong influence of the print bed temperature T_b on the crystalline state of the PLA components. Interestingly, the degree of crystallinity χ_c for the PLA components printed at T_b = 30 °C shows a strong decrease for heights z $\geq$ 15 mm approaching the top of the full part of the component at z = 20 mm. This effect is reproducible and much less pronounced for components printed at higher print bed temperature T_b (60 and 90 °C). This indicates that the heat transferred from the subsequently printed layers has a significant effect on the degree of crystallinity χ_c. This applies in particular to components printed at print bed temperatures T_b below the glass transition temperature T_g of PLA. Note that this finding is confirmed by WAXD measurements on horizontal sections taken close to the top of the unfilled part ($z \approx 20$ mm).

Depth-dependent WAXD studies are performed similar to that for PA12 components.

Figure 12(a) shows representative scattering pattern taken at a depth of $x = 2.5$ mm for PLA components printed at different print bed temperatures. Like in height dependent WAXD studies the orthorhombic α phase is commonly observed independent on print bed temperature T_b and depth x. This is evidenced by the characteristic reflections labeled in Figure 12(a).

Figure 12(b) shows data for the degree of crystallinity χ_c at print bed temperatures T_b of

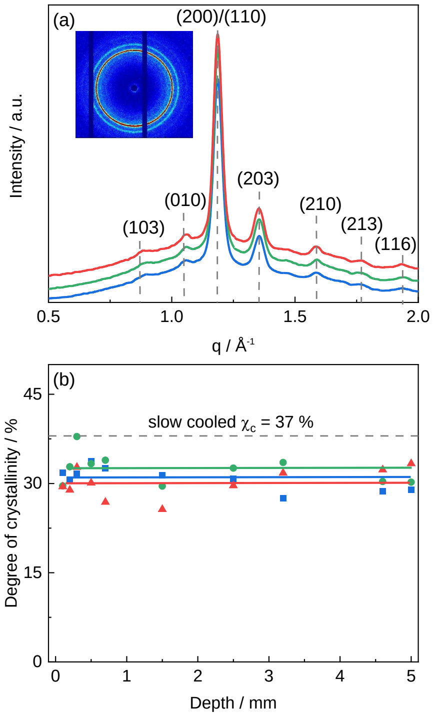

Figure 12: (a) Representative 1D WAXD scattering pattern of PLA components printed at T_b = 30 °C, 60 °C and 90 °C at a depth of $x = 2.5$ mm (fixed $z = 10$ mm and $y = 15$ mm). The inset shows a representative 2D scattering pattern (T_b = 30 °C) exhibiting isotropic intensity distribution. (b) Degree of crystallinity χ_c as function of the depth x of 3D-printed PLA components prepared at print bed temperatures T_b of 30 °C (blue squares), 60 °C (green circles) and 90 °C (red triangles). The degree of crystallinity χ_c of slowly cooled PLA is indicated by a dashed line.

30 °C, 60 °C and 90 °C as function of depth x. In contrast to the χ_c values from the height dependent scans the degree of crystallinity χ_c remains here constant. It is scattering around 30% nearly, irrespective of print bed temperature T_b and depth x. This indicates that the heat transferred to the print bed or from subsequently printed layers is most relevant for

the crystalline state appearing in 3D-printed PLA components. Hence, the position within a layer seems to be less relevant for χ_c.

The structural parameters from peak fitting are listed in Table 4. The values at print bed temperatures T_b of 60°C and 90°C are in good agreement with the data from height-dependent scans performed at similar height ($z = 2.5$ mm *vs.* $z = 10$ mm) while differences are seen for $T_\mathrm{b} = 30$°C since the height difference shows a much stronger influence in this case.

Semi-crystalline structure of 3D printed single layers

Figure 13(a) presents representative azimuthal integrated 1D scattering pattern of 3D-printed PA12 single layers printed at print bed temperatures T_b of 30 °C, 80 °C and 120 °C taken at a depth of $x = 0.75$ mm ($y = 15$ mm). The depth-dependent scans are carried out over the entire depth from 0 mm $\leq x \leq =$ 15 mm in steps of 0.75 mm ($y = 15$ mm). The 1D scattering pattern show two reflections in the low q region range at $q_{002} = 0.42$ Å^{-1} and $q_{004} = 0.79$ Å^{-1} and a major reflection in the WAXD region at $q_{100} = 1.51$ Å^{-1}. The corresponding d-spacing is $d_{100} = 4.16$ Å. The 1D scattering pattern of PA12 single layers are qualitatively similar to those of the γ phase obtained in temperature-dependent WAXD scans at 30 °C. This leads to the conclusion, that the γ phase of PA12 is the preferred phase in the single layers, quasi-independent on the print bed temperature T_b.

The peak fitting analysis is performed with a two peak fit similar as for the γ phase in temperature-dependent WAXD scans to obtain the area and $FWHM$ of the amorphous halo A_amo and the Bragg reflection A_cry, $FWHM_\mathrm{cry}$, respectively. The obtained values for q_{100}, d_{100}, L_{100} and the average degree of crystallinity $\overline{\chi}_\mathrm{c}$ are given in Table 5 and are in good agreement with values from temperature-dependent measurements. Figure 13(b) shows representative azimuthal integrated 1D scattering pattern of the PLA single layers, printed at print bed temperatures T_b of 30 °C, 60 °C and 90 °C. The PLA single layers printed at print bed temperatures T_b of 30 °C and 60 °C are completely amorphous over the

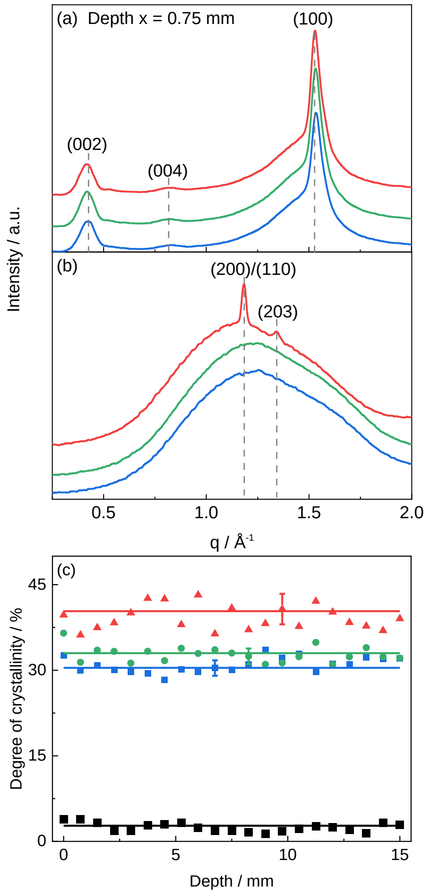

Figure 13: (a) Representative 1D scattering pattern for PA12 single layers for print bed temperatures of T_b = 30 °C, 80 °C and 120 °C. (b) 1D scattering pattern for PLA single layers, printed at print bed temperatures T_b of 30 °C, 60 °C and 90 °C. The 1D scattering pattern are obtained at a depth of $x = 0.75$ mm ($y = 15$ mm). (c) Corresponding degree of crystallinity χ_c as function of depth x for PA12 single layers as well as for a PLA single layer printed at $T_\mathrm{b} = 90$°C (black squares). The average degree of crystallinity $\overline{\chi}_\mathrm{c}$ is indicated by dashed lines for each data set along with the error bar being the standard derivation.

Table 5: Fit parameters for 3D-printed PA12 single layers at $x = 2.5$ mm and $y = 15$ mm

T_b [°C]	q_{100} [$\mathrm{Å}^{-1}$]	d_{100} [Å]	L_{100} [Å]	$\overline{\chi}_\mathrm{c}$ [%]	$\pm\,\overline{\chi}_c$ [%]
30	1.52	4.14	107.2	37	± 2
80	1.54	4.09	109.3	37	± 3
120	1.53	4.11	110.4	42	± 1

entire depth x range between $0\ \mathrm{mm} < x < 15\ \mathrm{mm}$ (at $y = 15\ \mathrm{mm}$). The PLA single layers printed at a print bed temperature T_b of 90 °C show weak but prominent reflections of the (200)/(110) and (203) planes at $q_{200/110} = 1.18\ \text{Å}^{-1}$ and $q_{203} = 1.43\ \text{Å}^{-1}$. The corresponding d-spacings are $d_{200/110} = 5.32$ Å and $d_{203} = 4.39$ Å, i.e., PLA is present in the orthorhombic α phase. Compared to temperature, height and depth-dependent WAXD scans, the intensity of the Bragg reflections is much weaker and less reflections are observed. The average degree of crystallinity $\overline{\chi}_\mathrm{c}$ of the PLA single layer at a print bed temperature T_b of 90 °C is 5 % ± 2.5 % and is thus much lower as compared with the degree of crystallinity χ_c of 3D-printed components (about 30 %).

In Figure 13(c) the degree of crystallinity χ_c of the PA12 single layers printed at print bed temperatures T_b of 30 °C, 80 °C and 120 °C is given as function of depth x. The average degree of crystallinity $\overline{\chi}_\mathrm{c}$ at print bed temperatures T_b of 30 °C and 80 °C are 36 % and 37 % and are in the same range as corresponding values from temperature-dependent measurements for PA12. The average degree of crystallinity $\overline{\chi}_\mathrm{c}$ of the PA12 single layer printed at a print bed temperature T_b of 120 °C is slightly higher (about 42 %). However, the observed deviation is within the experimental uncertainties.

In contrast to the depth-dependent 2D scattering pattern of the 3D-printed components shown above, all reflections show basically a isotropic intensity distribution.

Discussion

Factors causing inhomogeneities in the semi-crystalline state of 3D-printed components

Formation of inner surfaces: crystallization times *vs.* processing times

There are several factors influencing the semi-crystalline state of 3D-printed components. Of major importance is the selection of the crystallizable polymer. However, the final semi-crystalline state is also heavily affected by the processing conditions like local cooling rate and shear field. Both factors have to be considered in obtaining components made from semi-crystalline polymers with optimum properties and are also most relevant for the occurrence of inhomogeneities in the crystalline state. This applies to semi-crystalline polymeric components in general but in particular to 3D-printed components.

It is expected that material-related aspects and processing conditions are strongly interconnected in case of 3D-printing. On one hand, the local cooling rate applied to the molten polymer strand attached to the upper surface of an emerging component is influenced by processing parameters like nozzle temperature T_n, print bed temperature T_b, chamber temperature, processing speed v (repetition times) as well as dimensions of the component. On the other hand, there are material related influencing factors like crystallization kinetics, heat conductivity and heat capacity.

From a technical point of view extremely relevant are times defined by the FDM printing program like repetition times in-plane $t_\mathrm{r,ip}$ (time it takes to reach again a directly neighbored volume element within one layer) and repetition times out-of-plane $t_\mathrm{r,op}$ (time it takes to pass a directly neighbored volume element in next layer). These processing related times, $t_\mathrm{r,ip}$ and $t_\mathrm{r,op}$, should determine the interfacial situation to a large extend, i.e., whether or not pronounced interfaces/interphases develop between two neighbored volume elements in a component due to differences in the semi-crystalline state. To understand and quantify these effects it is important to compare the processing related repetition times, $t_\mathrm{r,ip}$ and $t_\mathrm{r,op}$, with crystallization times τ_c for the chosen polymers.

Figure 14 shows typical repetition times of the used printing program in comparison with crystallization times τ_c from isothermal crystallization measurements by calorimetry as function of temperature T for Renkforce © PLA and Fiberlogy © PA12. Selected results from literature are given for comparison. Print bed temperatures T_b and nozzle temperature T_n are indicated by vertical dashed lines, repetition times in-plane $t_\mathrm{r,ip}$ and out-of-plane $t_\mathrm{r,op}$ by horizontal lines. In case of PLA, crystallization is commonly slow. The crystallization times τ_c of PLA are significantly longer (at least ten times) than the repetition times $t_{r,ip}$ and $t_{r,op}$ in the entire temperature range between nozzle T_n and print bed temperature T_b. One can conclude that crystallization of one volume element will not be completed before a neighbored volume element is printed beside ($t_{r,ip}$) or on top ($t_{r,op}$). When looking at crystallization times for PA12, it can be seen that PA12 crystallizes much faster compared to PLA. The comparison in Figure 14(b) shows clearly that crystallization is completed at all investigated print bed temperatures T_b (30 °C$\leq T_b \leq$ 120 °C) before a new volume element is attached in- and out-of-plane. Only at very high temperatures ($T >$ 150 °C) crystallization times τ_c are longer than relevant processing times $t_{r,ip}$ and $t_{r,op}$. To obtain a homogeneous component minimum differences in the semi-crystalline state, crystallization times τ_c should be longer than repetition times in- and out-of-plane in order to prevent crystallization before neighbored volume elements are printed. This scenario might be also achievable for PA12 but only above a temperature T of 150 °C. Conclusion of this comparison is that only for high

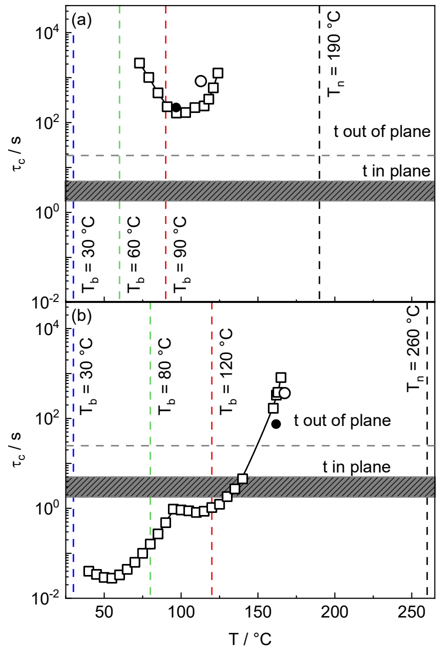

Figure 14: Crystallization times τ_c as function of temperature T for (a) PLA and (b) PA12. Nozzle temperature T_n (black) and bed temperatures T_b (colored) are shown as vertical dashed lines. Repetition times $t_{r,ip}$ and $t_{r,op}$ are indicated with horizontal lines. Crystallization times τ_c derived from non-isothermal crystallization experiments on PLA[33] and PA12[34] in the literature are also given (closed circle 5 K/min and open circle 1 K/min)

print bed T_b and environmental temperatures situations can be achieved for PA12 which are similar to the conditions that commonly exist for slowly crystallizing PLA.

The experimental findings of this work support the predictions derived based on Figure 14 and provide further insights. The properties of "isothermally printed components", i.e., single layers from PLA as considered in Figures 13, are in line with relations between crystallization τ_c and processing times $T_\mathrm{r,ip}$ and $t_\mathrm{r,op}$ highlighted in Figure 14. PLA single layers do not show crystallinity at print bed temperatures $T_\mathrm{b} \leq 90$ °C. This can be understood as a consequence of long crystallization times $\tau_c > 150$ s for all temperatures ≤ 90°C. Since printing time $t_\mathrm{r,op}$ of a single layer (18 s) is much shorter, one can conclude that crystallization can not take place before finishing one layer. The very weak degree of crystallinity χ_c obtained for the single PLA layer printed at $T_\mathrm{b} = 90$ °C is somehow expected since the crystallization time τ_c is shortest for this temperature.

The fact that 3D-printed PLA components do show much higher crystallinities away from the print bed ($z > 5$ mm) for all investigated print bed temperatures T_b (Figure 11) can be interpreted as a consequence of crystallization forced by heat induced by molten material printed on top and by annealing of the component for the time needed to print the entire component layer by layer (3300 s). The temperature in the core region is probably higher resulting in faster crystallization and in a lower effective cooling rate since the heat introduced by hot material during printing of subsequent layers is not transported from the core of the component to its outer surfaces or to the print bed due to poor heat conductivity of polymers. Due to the generally slow crystallization kinetics of PLA, a reduction in the degree of crystallinity χ_c is for PLA components mainly seen close to the print bed at $T_\mathrm{b} \leq$ 60 °C where heat can be transferred effectively to the print bed. Away from that region PLA components exhibit high homogeneity, as crystallization takes place very slowly after several layers have been already printed on top (at least eight layers when assuming a crystallization time τ_c of 150 s). In contrast to PLA, PA12 crystallizes much faster under all conditions investigated. The crystallization times τ_c are for all print bed temperatures T_b significantly shorter than the printing time $t_{\mathrm{r,op}}$ required for one single layer (18 s) as confirmed by the high degree of crystallinity χ_{c} of PA12 single layers printed at print bed temperatures T_{b} in the range of 30 °C $\leq T_{\mathrm{b}} \leq$ 120 °C (Figure 11 (a)). The crystallization times τ_{c} below 150 °C are also faster than all repetition times $t_{\mathrm{r,ip}}$ and $t_{\mathrm{r,op}}$. This explains why distinct interfaces between different layers are observed for PA12 components printed at bed temperatures T_{b} $\leq$ 120 °C in POM images (see Figures SI6 to SI9). Crystallization of one layer is completed before the next layer is printed in these cases. This feature disappears only in the core of the component for $T_{\mathrm{b}} \geq$ 80 °C possibly since the heat introduced by the hot melt leads here together with poor heat conductivity to really high crystallization temperatures in the core region close to 150 °C during 3D-printing. The finding that a certain fraction of α phase is seen in 3D-printed PA12 components supports the idea that crystallization temperatures above 135 °C (being the monoclinic (α/α') to hexagonal (γ/γ') transition temperature) occur during printing of the component.

Crystal orientation effects: terminal relaxation time vs. crystallization time

Another effect that can be at least partly explained based on the experimental results presented in this work are differences regarding crystal orientation. For that purpose it seems to be important to consider the ratio of terminal relaxation time to crystallization time $\tau_{\mathrm{r}}/\tau_{\mathrm{c}}$. This ratio is plotted as function of temperature T in Figure 15 for PLA and PA12. Also for this quantity prominent differences between PLA and PA12 are observed. Isothermal crystallization is for PLA obviously always slower than terminal relaxation (onset of flow) while this case occurs for PA12 only at high temperatures above 150 °C. At all lower temperatures crystallization is much faster than terminal relaxation. This can explain qualitatively why orientation is commonly absent in 3D-printed PLA components but partly seen for (the α phase of) PA12. Main reason which is causing crystal orientations in 3D-printed components should be shear induced in the nozzle region. Since the strands are sheared within the nozzle, polymer chains are stretched and thus potentially oriented during deposition on bed or component surface. A ratio $\tau_r/\tau_c < 1$ means that the polymer chains have enough time to reach a relaxed state before crystallization. A ratio $\tau_r/\tau_c > 1$ means that relaxation can not take place before crystallization which is resulting in remaining orientation. In case of PA12 chain relaxation can only take place at temperatures above 150 °C before crystallization occurs. Since α crystals in PA12 components are oriented it can be speculated that the temperature on the upper surface of components was always below 150 °C. Note that we consider here moderate shear rates where the influence of shear rate $\dot{\gamma}$ on the flow behavior can be still neglected. In summary, one can conclude that in order to obtain an interface free, more homogeneous and non-oriented microstructure of PA12 components, it would be reasonable to print at print bed temperatures T_b above 150 °C mimicking the general situation in PLA.

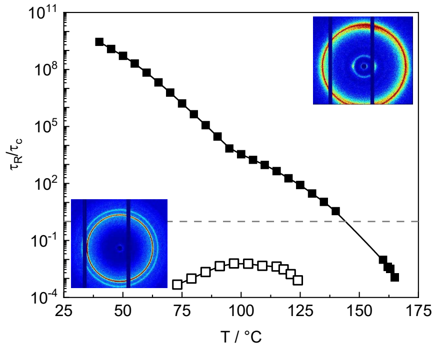

Figure 15: Ratio of relaxation times to crystallization times $\tau_\mathrm{r}/\tau_\mathrm{c}$ as function of temperature T of PLA (open squares) and PA12 (closed squares). The dashed line is indicating that relaxation time τ_r is longer than crystallization time τ_r.

Macroscopic void formation: Terminal relaxation times vs. processing times

To achieve compact components without macroscopic voids it is important to know the flow behavior of 3D-printing materials. In the previous section, the influence of terminal relaxation time τ_r on the semi-crystalline state within a component has been already discussed. However, the knowledge of terminal relaxation time is also important to choose the right printing program from the viewpoint of macroscopic void formation and defects. In the literature sometimes criteria based on viscosity are used, e.g. the zero shear viscosity η_0 about

10^2 to 10^3 $\mathrm{Pa} \cdot \mathrm{s}$.[16–20] The, terminal relaxation time τ_r is an alternative since it indicates the transition from rubbery state to liquid state. Somehow, this is a more robust quantity since well defined viscosities are often hard to get for commercial polymers at application relevant temperatures. The rubber to liquid transition is not sharp but a continuous transition since (in particular for commercial grades with broad molecular weight distribution) relaxation features (flow transition) play an important role in this range. Figure 16 presents terminal relaxation times τ_r for PLA and PA12 as function of temperature T in comparison with in- and out-of-plane repetition times $t_\mathrm{r,ip}$ and $t_\mathrm{r,op}$. To extend the temperature interval, terminal relaxation times obtained from dynamic mechanical measurements are extrapolated based on the Arrhenius law. The temperature dependence of PA12 is seemingly more pronounced compared to that of PLA and the terminal relaxation time τ_r at the nozzle temperature T_n is significantly shorter (indicating lower viscosity η). In principle, the molten filament strand should flow only for a certain time period after deposition on the surface of the component.

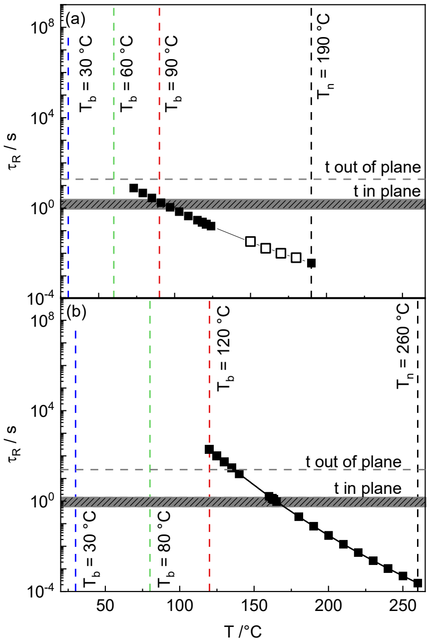

Figure 16: Terminal relaxation times τ_r as function of temperature T for (a) PLA and (b) PA12 obtained from dynamic mechanical measurements (open squares). Extrapolated terminal relaxation times τ_r (filled squares) obtained by an Arrhenius fit. Printing times in-plane and out-of-plane, $t_\mathrm{r,ip}$ and $t_\mathrm{r,op}$, are indicated by horizontal lines. Nozzle T_n and print bed temperatures T_b are indicated with vertical dashed lines.

Which shape is observed and to what extend void formation can be excluded depends to a large extent on the cooling behavior. Flow stops if a temperature is reached where the terminal relaxation times τ_r are too long or if crystallization occurs. In a way one can argue that temperatures where $\tau_\mathrm{r} > t_\mathrm{r,ip}$ should be irrelevant 3D-printing conditions since an appropriately shaped strand on the surface should be formed before the nozzle is printing the next strand beside. Strand shaping on the surface should definitively be completed above that temperature where $\tau_\mathrm{r} = t_\mathrm{r,ip}$ (120 °C for PLA, 175 °C for PA12, cf. Figure 16) if shear rate dependent effects are neglected. Crystallization during cooling will appear under application relevant conditions at lower temperature for both polymers. Importantly, all the details depend on local cooling rate.

Insufficient flow can lead to processing errors such as macroscopic voids. Henceforth, to avoid voids and get a smooth surface it is important to optimize the flow behavior of polymeric filaments knowing the relevant conditions of the 3D-printing process.

Conclusions

Summarizing the above discussion about influencing factors, one can conclude that producing 3D-printed components with a small number of intrinsic interfaces and homogeneous semi-crystalline structure requires a detailed knowledge of terminal relaxation and crystallization times (τ_r, τ_c) of the used material and processing related times like repetition times in- and out-of-plane ($t_\mathrm{r,ip}$ and $t_\mathrm{r,op}$). For 3D-printed components with optimal properties different ratios of these times should be considered or incorporated in numerical simulations in order to find suitable strategies to improve component quality. In particular one should consider the following guidelines:

1.) to get a spatially uniform semi-crystalline state without pronounced interfaces within a component one should tune the repetition times (within a layer or layer-to-layer) during printing in such a way that repetition times ($t_\mathrm{r,ip}$ and $t_\mathrm{r,op}$) are shorter than crystallization times $\tau_\mathrm{c}(T,\, \dot{\gamma})$ under printing conditions; considering that the printing speed v should be adapted ideally to the crystallization kinetics of the chosen material (or vice versa e.g. by adding/removing nucleating agents to/from the used polymer).

2.) to avoid anisotropy of the semi-crystalline structures within a 3D-printed component one should chose printing conditions where the ratio $\tau_\mathrm{r}/\tau_\mathrm{c}$ is smaller than one; this means that shear stresses can relax to a large extent before crystallization begins; the situation can be influenced e.g. by temperature conditions and molecular weight of the chosen polymer or additivation.

3.) to prevent void formation and related defects of 3D-printed components one should chose printing conditions which fit to the terminal relaxation time τ_r and overall flow behavior of the polymer filament used; the nozzle temperature T_n is important here, the shape of the strands formed on the component surface depends on it, but also the subsequent cooling process and the shear field in the nozzle are important; process-based strategies to improve the situation are changes in nozzle T_n, print bed T_b and chamber temperature or a material-based approach focusing for example on the optimization of the molecular weight distribution.

These guidelines show that for a problem-specific optimization a detailed knowledge of relevant material properties, cooling conditions and shear introduced in the nozzle are important. While material related parameters can be measured by suitable methods, the process specific information can in detail only be provided by numerical simulations. Therefore suitable input parameters should be determined and used in order to be able to chose optimized materials and processing conditions for each individual polymeric component to be produced by FDM.

References

(1) Durach, C.; Kurpjuweit, S.; Wagner, S. The impact of additive manufacturing on supply chains. *International Journal of Physical Distribution & Logistics Management* **2017**,

47, 954–971.

(2) Petschow, U.; Ferdinand, J.-P.; Dickel, S.; Flämig, H.; Steinfeldt, M.; Worobei, A. Dezentrale Produktion, 3D-Druck und Nachhaltigkeit. *Schriftenreihe des IÖW 206/14* **2014**, 1–58.

(3) Costanzo, A.; Croce, U.; Spotorno, R.; Fenni, S. E.; Cavallo, D. Fused Deposition Modeling of Polyamides: Crystallization and Weld Formation. *Polymers* **2020**, *12*, 2980.

(4) de Jager, B.; Moxham, T.; Besnard, C.; Salvati, E.; Chen, J.; Dolbnya, I. P.; Korsunsky, A. M. Synchrotron X-ray Scattering Analysis of Nylon-12 Crystallisation Variation Depending on 3D Printing Conditions. *Polymers* **2020**, *12*, 1169.

(5) Qi, S.; Gao, X.; Su, Y.; Dong, X.; Cavallo, D.; Wang, D. Correlation between welding behavior and mechanical anisotropy of long chain polyamide 12 manufactured with fused filament fabrication. *Polymer* **2021**, *213*, 123318.

(6) Wang, L.; Gramlich, W. M.; Gardner, D. J. Improving the impact strength of Poly(lactic acid) (PLA) in fused layer modeling (FLM). *Polymer* **2017**, *114*, 242–248.

(7) Liao, Y.; Liu, C.; Coppola, B.; Barra, G.; Di Maio, L.; Incarnato, L.; Lafdi, K. Effect of Porosity and Crystallinity on 3D Printed PLA Properties. *Polymers* **2019**, *11*, 1487.

(8) Srinivas, V.; van Hooy-Corstjens, C. S.; Harings, J. A. Correlating molecular and crystallization dynamics to macroscopic fusion and thermodynamic stability in fused deposition modeling; a model study on polylactides. *Polymer* **2018**, *142*, 348–355.

(9) Kawai, T.; Rahman, N.; Matsuba, G.; Nishida, K.; Kanaya, T.; Nakano, M.; Okamoto, H.; Kawada, J.; Usuki, A.; Honma, N.; Nakajima, K.; Matsuda, M. Crystallization and Melting Behavior of Poly (L-lactic Acid). *Macromolecules* **2007**, *40*, 9463–9469.

(10) Wasanasuk, K.; Tashiro, K. Crystal structure and disorder in Poly(L-lactic acid) δ form (α' form) and the phase transition mechanism to the ordered α form. *Polymer* **2011**, *52*, 6097–6109.

(11) Lohmeijer, P. J. A.; Goossens, J. G. P.; Peters, G. W. M. Quiescent crystallization of poly(lactic acid) studied by optical microscopy and light-scattering techniques. *Journal of Applied Polymer Science* **2017**, *134*, 44566.

(12) Ramesh, C. Crystalline Transitions in Nylon 12. *Macromolecules* **1999**, *32*, 5704–5706.

(13) Li, L.; Koch, M. H. J.; de Jeu, W. H. Crystalline Structure and Morphology in Nylon 12: A Small- and Wide-Angle X-ray Scattering Study. *Macromolecules* **2003**, *36*, 1626–1632.

(14) Dencheva, N.; Nunes, T. G.; Oliveira, M. J.; Denchev, Z. Crystalline structure of polyamide 12 as revealed by solid-state 13C NMR and synchrotron WAXS and SAXS. *Journal of Polymer Science Part B: Polymer Physics* **2005**, *43*, 3720–3733.

(15) Fischer, C.; Seefried, A.; Drummer, D. Crystallization and Component Properties of Polyamide 12 at Processing-Relevant Cooling Conditions. *Polymer Engineering & Science* **2017**, *57*, 450–457.

(16) Verbelen, L.; Dadbakhsh, S.; Van den Eynde, M.; Kruth, J.-P.; Goderis, B.; Van Puyvelde, P. Characterization of polyamide powders for determination of laser sintering processability. *European Polymer Journal* **2016**, *75*, 163–174.

(17) Arrigo, R.; Frache, A. FDM Printability of PLA Based-Materials: The Key Role of the Rheological Behavior. *Polymers* **2022**, *14*, 1754.

(18) Patti, A.; Acierno, S.; Cicala, G.; Acierno, D. Predicting the Printability of Poly(Lactide) Acid Filaments in Fused Deposition Modeling (FDM) Technology: Rheological Measurements and Experimental Evidence. *ChemEngineering* **2023**, *7*, 1.

(19) O'Mahony, C.; Gkartzou, E.; Haq, E. U.; Koutsoumpis, S.; Silien, C.; Charitidis, C. A.; Tofail, S. A. M. Determination of thermal and thermomechanical properties of biodegradable PLA blends: for additive manufacturing process. *Journal of Thermal Analysis and Calorimetry* **2023**, *142*, 715–722.

(20) Ou-Yang, Q.; Guo, B.; Xu, J. Preparation and Characterization of Poly(butylene succinate)/Polylactide Blends for Fused Deposition Modeling 3D Printing. *ACS Omega* **2018**, *3*, 14309–14317.

(21) Xenopoulos, A.; Wunderlich, B. Heat capacities of solid polyamides. *Polymer* **1990**, *31*, 1260–1268.

(22) Pyda, M.; Bopp, R.; Wunderlich, B. Heat capacity of poly(lactic acid). *The Journal of Chemical Thermodynamics* **2004**, *36*, 731–742.

(23) Jariyavidyanont, K.; Du, M.; Yu, Q.; Thurn-Albrecht, T.; Schick, C.; Androsch, R. Bulk Enthalpy of Melting of Poly (L-lactic acid) (PLLA) Determined by Fast Scanning Chip Calorimetry. *Macromolecular Rapid Communications* **2022**, *43*, 2200148.

(24) Jariyavidyanont, K.; Schick, C.; Androsch, R. The bulk enthalpy of melting of α'-crystals of poly (L-lactic acid) determined by fast scanning chip calorimetry. *Thermochimica Acta* **2022**, *717*, 179349.

(25) Gogolewski, S.; Czerntawska, K.; Gastorek, M. Effect of annealing on thermal properties and crystalline structure of polyamides. Nylon 12 (polylaurolactam). *Colloid and Polymer Science* **1980**, *280*, 1130–1136.

(26) Ferry, J. *Viscoelastic Properties of Polymers*; Wiley, 1980.

(27) Zhang, R.; Du, F.; Jariyavidyanont, K.; Zhuravlev, E.; Schick, C.; Androsch, R. Glass transition temperature of poly(D,L-lactic acid) of different molar mass. *Thermochimica Acta* **2022**, *718*, 179387.

(28) Inoue, K.; Hoshino, S. Crystal structure of nylon 12. *Journal of Polymer Science: Polymer Physics Edition* **1973**, *11*, 1077–1089.

(29) Dosière, M. Orientation of the lamellar crystals in polyamide 12. *Polymer* **1993**, *34*, 3160–3167.

(30) Rhee, S.; White, J. L. Crystal Structure and Morphology of Biaxially Oriented Polyamide 12 Films. *Journal of Polymer Science: Part B: Polymer Physics* **2002**, *40*, 1189–1200.

(31) Dai, R.; Huang, M.; Ma, L.; Liu, W.; He, S.; Liu, H.; Zhu, C.; Wang, Y.; Zhang, Z.; Sun, A. Study on crystal structure and phase transitions of polyamide 12 via wide-angle X-ray diffraction with variable temperature. *Advanced Composites and Hybrid Materials* **2020**, *3*, 522–529.

(32) Hiramatsu, N.; Haraguchi, K.; Hirakawa, S. Study of Transformations among α, γ and γ' Forms in Nylon 12 by X-Ray and DSC. *Japanese Journal of Applied Physics* **1983**, *22*, 335.

(33) Liu, Y.; Wang, L.; He, Y.; Fan, Z.; Li, S.-M. Non-isothermal crystallization kinetics of poly(L-lactide). *Polymer International* **2010**, *59*, 1616–1621.

(34) Zhao, M.; Wudy, K.; Drummer, D. Crystallization Kinetics of Polyamide 12 during Selective Laser Sintering. *Polymers* **2018**, *10*, 168–182.